Research Article

Effect of CuO, MoO_3 and ZnO nanomaterial coated absorbers for clean water production

T. Arunkumar[1] · D. Murugesan[2] · C. Viswanathan[2] · G. Neri[3] · David Denkenberger[4]

Received: 18 May 2020 / Accepted: 11 September 2020 / Published online: 18 September 2020

Abstract

Solar energy is one of the most powerful sources for many sustainable applications. Recently, efficient water distillation has attracted significant attention. The fresh water productivity depends on how efficiently the system harvests the incoming solar energy and converts it into useful heat. In the present work, nano-coated absorber plates (NCAPs) were examined in the single slope solar still (SSSS) for clean water production. The NCAPs were CuO, MoO_3 and ZnO, respectively. The CuO-NCAP was fabricated with the thermal evaporation method while the radio-frequency Magnetron Sputtering technique was used to fabricate the MoO_3 and ZnO NCAPs. The attained particle size of the CuO, MoO_3 and ZnO are 30–34 nm, 25–30 nm and 30–35 nm, respectively. The sphere (CuO), plate (MoO_3), and wedge (ZnO) like morphologies are identified with field emission-scanning electron microscope. All the NCAPs and reference solar still were tested under the same environmental conditions. The climatic parameters (solar influx, ambient temperature and wind) and SSSS's temperatures including water temperature (T_w), internal air temperature ($T_{int\text{-}air}$), inner cover (T_{ic}), outer cover (T_{oc}), and absorber plate temperature (T_{NCAP}) were measured at 30 min intervals with the help of Type-J thermocouples. Herein, we present an evaporative heat transfer (h_{ew}), efficiency, and cost analysis of the SSSS with CuO, MoO_3 and ZnO-NCAPs. Three different feed waters fetched from the surface well water, hill side well water and hill side pond water were used in this work for evaporation. The result reveals that the evaporation of conventional single slope solar still, CuO, MoO_3 and ZnO NCAPs were 2.1 l/m^2 day, 2.9 l/m^2 day, 2.7 l/m^2 day and 2.6 l/m^2 day, respectively.

Keywords Nano material · Solar still · Solar radiation · Heat transfer · Vapour generation

List of symbols

A	Area of the basin (m^2)
D	Crystallite size (nm)
I	Incident solar influx (W/m^2)
h	Heat transfer coefficient (W/m^2 K)
k	Shape factor
L	Latent heat of vaporization (J/kg)
M	Mass of the output water
P	Partial pressure (N/m^2)
U	Wind velocity (m/s)
T	Temperature (°C)
t	Time (s)

Greek symbols

α	Absorptivity
β	Full width-half maximum
ε	Emissivity

Electronic supplementary material The online version of this article (https://doi.org/10.1007/s42452-020-03504-5) contains supplementary material, which is available to authorized users.

✉ G. Neri, gneri@unime.it | [1]National Center for International Research on Photoelectric and Energy Materials, Yunnan Provincial Collaborative Innovation Center of Green Chemistry for Lignite Energy, Yunnan Province Engineering Research Center of Photocatalytic Treatment of Industrial Wastewater, The Universities' Center for Photocatalytic Treatment of Pollutants in Yunnan Province, School of Chemical Sciences and Technology, Yunnan University, Kunming 650091, China. [2]Department of Nano-Science and Technology, Bharathiar University, Coimbatore, Tamilnadu 641 046, India. [3]Department of Engineering, University of Messina, 98166 Messina, Italy. [4]Mechanical Engineering and the Alaska Center for Energy and Power, University of Alaska Fairbanks, Fairbanks, AK, USA.

θ	Bragg's angle
σ	Steffen Boltzmann constant (5.67×10^{-8} W/m^2 K^4)

Subscripts

a, b, and c	Lattice parameters
amb	Ambient
b	Basin
c	Convection
e	Evaporation
h, k, and l	Miller's indices
ic	Inner cover
int-air	Internal-air
oc	Outer cover
w	Water
r	Radiation

Abbreviations

AFM	Atomic force microscopy
AMS	Air melamine sponges
BDL	Below detection level
BGNPs	Black gold nanoparticles
BW	Bubble wrap
CS	Carbon sponges
CSS	Conventional solar still
CSSSS	Conventional single slope solar still
EDS	Energy dispersive spectrum
EPF	Expanded polystyrene foam
FE-SEM	Field emission-scanning electron microscope
KM plots	Kubelka–Munk plots
HWW	Hill well water
HPW	Hill pond water
MIT	Massachusetts Institute of Technology
NCAP	Nanocoated absorber plate
NF	Nanofluid
NP	Nanoparticle
NR	No relaxation
PCM	Phase change material
PIL	Porous insulating layer
PM	Plasmonic membrane
SS	Solar still
SSSS	Single slope solar still
SSPCM	Shape stabilized phase change materials
SWW	Surface well water
TES	Thermal energy storage
UV	Ultraviolet spectra
WHO	World health organization
XRD	X-ray diffraction

1 Introduction

In recent decades, people have studied the effect of nanoparticles (NPs) as absorbers of solar energy in water evaporation systems. In traditional evaporation systems, the material's absorptivity is not well matched with the broadband incident solar radiation range. But the emergence of nano materials coupled with solar energy shows a pathway to improved wastewater and seawater evaporation systems. The coated NPs absorb the incoming solar energy and convert it into useful heat (photo-thermal conversion). The heat generated by the NPs is used to evaporate the wastewater/seawater for reuse. Nano energy (NPs + solar energy) have been used to evaporate the wastewater for desalination [37, 39, 65, 68, 69, 73].

These nano-enabled materials shift attention back towards the traditional solar-evaporation systems, simply called "solar stills" (SSs) [5–9, 11–13, 40, 42, 46, 53, 55] capable of producing more than 5 l/m^2 day [9, 11]. The effect of nano-coated condensation surface was developed to augment the evaporation in the solar still [71]. The result was concluded that the silicone nano-coated condensation cover was improved the freshwater productivity and yielded 5.8 kg/m^2/day. The graphene oxide nanoparticle with phase change material (NPCM) was used in the tubular solar still to improve the evaporation rate. The result was inferred that, the productivity of with and without NPCM was 2.59 and 5.62 kg/m^2/day [32]. Many researchers used real wastewaters in the solar still for purification. Tokumura et al. [61] experimentally studied the coffee waste water through solar light powered photo-Fenton reaction. The result concluded that the solar energy powered photo-Fenton process efficiently de-colorization the waste coffee effluent. Du et al. [18] investigated a removal of cytotoxicity through solar irradiation. The result reveals that the solar light reduced the cytotoxicity efficiently by 65% under 12 h of solar irradiation. Few other methods are involving the treatment of wastewater including zero-valent iron treatment [62], electrocoagulation-electro oxidation process [24], zinc-oxide nanoparticle [52], photo-Fenton reaction [60] and removal of Cr(VI) process [57]. The modified cotton cloth was used for different application in the research nowadays including water treatment [35, 67], $SiCl_4$ coated cotton cloth for oil removal [25], carbonized cotton cloth as supercapacitors [23, 64], removal of toxic dye reduction [2], and electro-catalyst and splitting [72].

Solar still can evaporate any kind of wastewater for purification. Researchers used sea water [70, 72], river water [20], industrial wastewater [20] and synthetic water [69] in the solar still. The water quality result

reveals that the parameters greatly improved after evaporation [22, 34, 51]. The sustainable cost-effective clean water production is the welcome addition for eco-friendly environment. Further, some recent investigations in the absorbing materials in the solar still are follows. Suneesh et al. [58] experimentally studied the double slope solar still with cotton cloth on the top cover. The cotton cloths were laid on the solar still's top cover to reduce the cover temperature. In this process, the evaporation rate was improved due to the temperature difference between the top cover and the basin liner was increased. Kabeel et al. [27, 28] experimentally studied the jute cloth knitted sand energy storage material in the solar still to augment the evaporation for desalination. The capillary action by the jute cloth and sand energy storage in the distiller were produced of 5.9 kg/m^2 day. Agrawal et al. [1] investigated the effect of jute cloth on the solar still basin to enhance the evaporation rate. Additionally, the jute cloths were laid on the vertical side of the solar still to improve the evaporation performance. The result was that the jute cloth enabled solar still enhanced the productivity of the distiller by 62%. Modi and Modi [41] studied the small pack of cotton cloth and jute material on the solar still. The productivity results concluded that the small pack of jute cloth shows the maximum productivity (0.9 L/m^2 day) than small pack of cotton cloths (0.9 L/m^2 day). Arjunan [4] experimentally investigated the solar still with cotton cloth energy storage for productivity enhancement. Four different cloths thickness including 2, 4, 6 and 8 mm were used in the solar still. The result elucidates that the 6 mm cotton cloth gives the best productivity and 24.1% freshwater improvement over conventional solar still.

Researchers have used nanomaterials coated on sponges [20] and directly mixed with water as NFs [10]. Herein, an attempt is made to study CuO, MoO_3 and ZnO-NPs coated on a stainless steel 316 (SS316) substrate. Many authors have done their research work in solar distillation to purify the wastewater. In order to augment the evaporation rate, efficient nano-structured materials were used in the solar distiller. In the present research, CuO, MoO_3 and ZnO nano-materials were coated on the substrate and investigated the evaporation rate enhancement. Researchers used nanomaterials in the solar distiller in the form of nano-fluids to improve the heat transfer rate. For the first time, the coated nanostructured materials were used in the solar distiller. Moreover, three different water samples, including surface well water (SWW) and other two samples were fetched from 4920 m high "*Palamalai mountain*" open pond water and open well water. For the first time, the water samples were collected from the high altitude location for the treatment process in the distiller. The NCAPs were characterized by X-ray diffraction (XRD), field emission scanning electron microscope (FE-SEM), energy dispersive spectrum (EDS) and corresponding colour mapping, UV–Vis spectroscopy, Raman spectroscopy, and atomic force microscope (AFM).

2 Experimental setup and procedure

Herein, four identical SSSSs were designed and fabricated at Institute for Energy Studies, Anna University, India. The effective absorber area of each of the SSSSs was 0.50 m^2. The vertical height of the sides are 0.35 m and 0.15 m, respectively. Transparent glass of thickness 3 mm was used for condensing for the SSSS with an angle of 11° from horizontal. The water level was replenished to 3 cm each day for the experiment [33]. The basin of the SSSS was painted black to enhance absorption. The CuO, MoO_3 and ZnO-NCAPs were 0.04 m × 0.04 m, respectively (30 plates/sample). The NCAPs are arranged randomly at the bottom of the SSSS. The walls and bottom of the SSSS were sealed with bubble wrap (BW) to reduce heat loss to the surroundings [8]. A measuring jar was used to collect the condensed water from the distiller in every 30 min. J-type thermocouples were used to measure the temperatures of the water, inner cover, outer cover, internal air, NCAP (as appropriate) and ambient, T_w, $T_{int\text{-}air}$, T_{ic}, T_{oc}, T_{NCAP}, and T_{amb}, respectively, at frequent time intervals (half an hour). Accuracy of the measuring instruments is shown in Table 1. The line diagram of the experimental arrangement is shown in Fig. 1. The BW insulated SS is shown in Fig. 2a, b.

Table 1 Accuracy of the measuring instruments

S. no.	Instrument	Model/make	Accuracy	Range
1	Data acquisition system	HP-Agilent 34970A	± 1 °C	0–100 °C
2	Pyranometer	HUKSEFLUX CP02	± 5 W/m^2	0–1750 W/m^2
3	J-type thermocouples	GENERIC	± 0.1 °C	0–100 °C
4	Anemometer	AVM-03	± 2%	0–9990 CFM
5	Measuring jar	Borosil	± 10 ml	0–1000 ml

BDL below detection level, *NR* no relaxation, *SWW* surface well water, *HWW* hill well water, *HPW* hill pond water

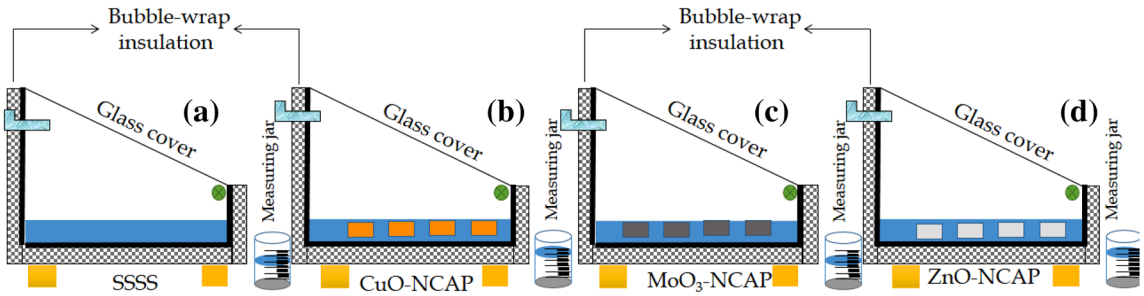

Fig. 1 Schematic view of CSS and CuO, MoO_3 and ZnO absorbers in the SSSS

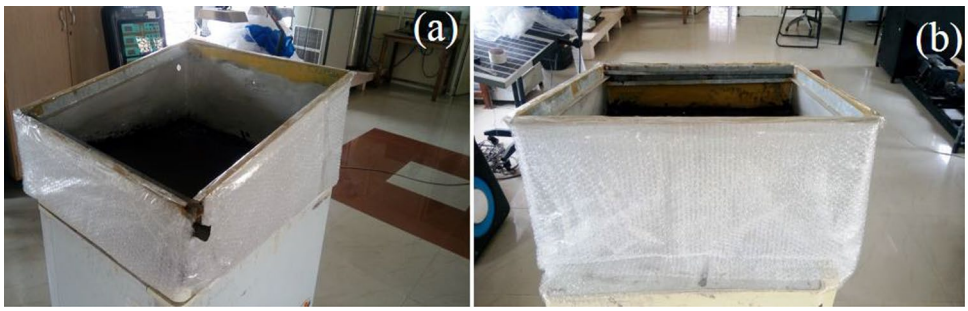

Fig. 2 Photo of SSSS with bubble wrap for experiment

3 Coating technique

All analytical grade chemicals were purchased from Himedia specialties and used without further purification. A 0.1 mm thick SS316 substrate and copper wire were purchased from local market, Coimbatore, Tamilnadu, India. The Cu, Mo and Zn metal target procured from Sigma Alrich (50 mm diameter and 3 mm thickness) with 99.999% purity.

The SS316 substrates were polished using emery papers of 400, 1000 and 1500 grit sizes, followed by washing with acetone and deionized water 2–3 times. Then the substrates were kept under sonication for 1 h and were kept in a hot air oven overnight to remove impurities and organic residues thoroughly. The substrates for MoO_3 and ZnO were placed in reactive radio frequency (RF) magnetron sputtering system from Huttenger, Germany in a customized down setup sputtering mode with Ar^+ (99.999%) used as working gas and O_2 (99.999%) as reactive gas in 1:5 ratios. The Mo metal target was fixed in the working pressure of 10^{-2} mbar for depositing a thin layer. The MoO_3 thin film seed layer thickness was 350 nm from a deposition rate of 3 Å/s at 450 °C substrate temperature. Similar, the Zn metal target use the same working pressure and the ZnO seed layer thickness was 300 nm with a deposition rate of 3 Å/s at 400 °C substrate temperature [63]. Here, the surface contamination on the target material was removed by pre-sputtering the target at 0.01 mbar for 10 min. The RF power for both MoO_3 and ZnO was 150 W and the distance between the target and substrate was maintained at 50 mm. Likewise, the physical-thermal evaporation method was used to coat the CuO on the SS316 substrates [9, 11].

4 Mechanism

The SS was properly insulated with the BW to trap the heat. The solar radiation strikes the SS and absorption takes place due to the blackened basin and NCAPs as applicable. The thermal energy is transferred by convective heat transfer to the basin water. This heat evaporates the water. Due to the temperature difference between the T_w and T_c, the evaporated water condenses on the cover and trickles down by gravity and is collected by the beaker. Adding nanomaterials

increases absorptivity in the basin, which increases the water temperature. Additionally, basin height [47], water depth [33], minimum glass temperature [44], and energy storage [16, 48] are key parameters involved in the productivity.

5 Material characterization

The crystal structure of the NCAPs were analysed by Grazing Incidence X-ray Diffraction (GI-XRD) (Rigaku—Ultima IV) with a monochromatic Cu-Kα_1 ($\lambda = 0.15406$ nm), having a scanning rate of 3°/min and 2θ range from 10° to 70°. Surface morphology was visualized by using FE-SEM (FEI, QUANTA 250) at an accelerating voltage of 20 kV. The topological and surface roughness was determined by AFM (Veeco di-caliber). Raman spectra were recorded using a Raman spectrometer (LABRAM-HR) with room temperature laser excitation ($\lambda = 514$ nm). The optical spectra were recorded using a UV–Vis spectrophotometer (JASCO, V-660), and Kubelka–Munk (KM) plots were obtained.

6 Results and discussion

The results and discussion comprises the findings of the XRD, FE-SEM, energy dispersive spectrum (EDS) and corresponding colour mapping, UV–Vis spectroscopy, Raman spectroscopy, AFM, effect of climatic parameters, recorded temperature variations in the solar still, recorded temperatures of NCAPs, evaporation rate, efficiency results, calculated heat transfer coefficients, physical and chemical water quality analyses, comparison of results with other related works and economic analysis.

6.1 XRD characterization

The XRD pattern of CuO coated NCAPs is shown in Fig. 3a. The diffraction peaks at 34.95° and 38.05° can be indexed to [002] and [111] planes of cubic phase; no other peaks were detected and well matched the standard data card (JCPDS file No: 45-0937) [9, 11]. The crystalline phase purity and structure of the MoO_3 are determined by XRD. The XRD patterns of the MoO_3 are shown in Fig. 3b. All the major diffraction peaks can be indexed to [020], [110], [040], [021], [111], [060], [200], [211] and [081] crystal

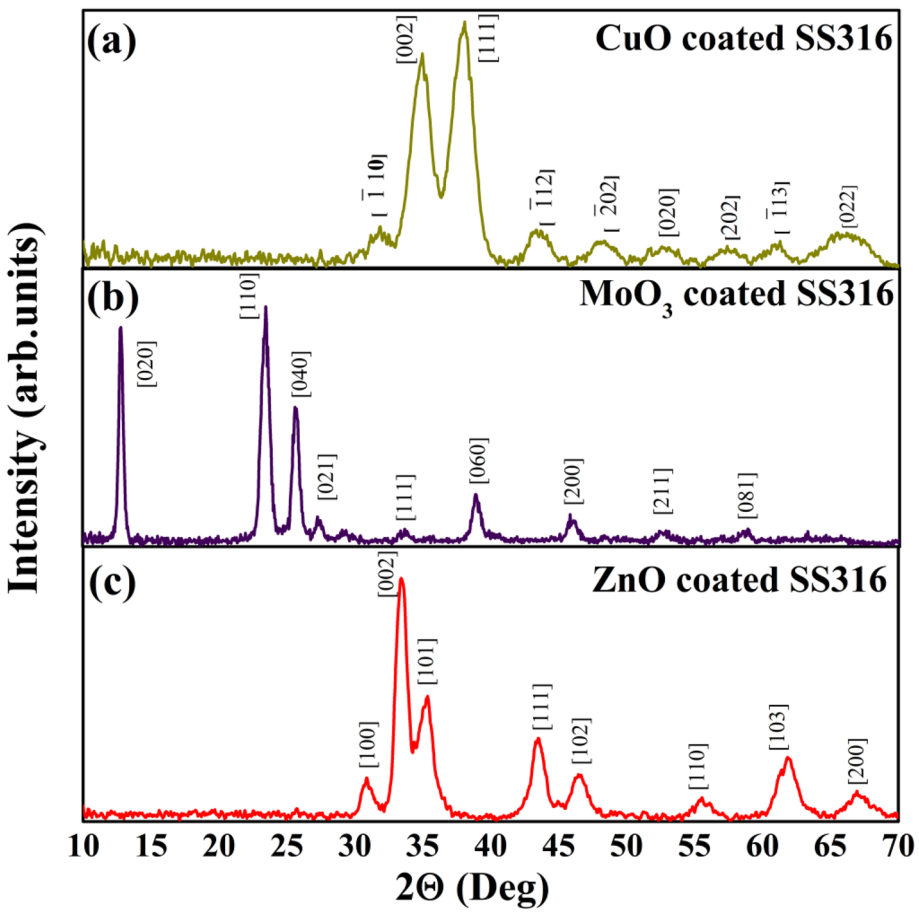

Fig. 3 XRD results of NCAPs **a** CuO coated SS316, **b** MoO_3 coated SS316, **c** ZnO coated SS316 (*arb* arbitrary)

planes. All the diffraction peaks are assignable to the orthorhombic phase of MoO_3 nanosheets (JCPDS NO 05-0508) obtained [43]. In addition, the X-ray diffraction peak intensities reveal different growth directions due to the fact that the substrate temperature of 450 °C produces highly crystalline single-phase orthorhombic MoO_3. Moreover, the XRD patterns of the ZnO coated SS316 nanostructured thin films is shown in Fig. 3c. All peaks can be well indexed to the wurtzite hexagonal phase of ZnO (JCPDS 36-1451) and no impurity phases are observed [3]. The sharp and strong peaks indicate that both samples have good crystalline nature.

The crystallite size (D) was calculated according to the Scherer's equation

$$D = \frac{k\lambda}{\beta \cos\theta} \tag{1}$$

where '*k*' is the shape factor, '*λ*' is the X-Ray wavelength, '*β*' is the full width at half maximum and '*θ*' is the Bragg angle. The attained crystal size of the CuO, MoO_3 and ZnO are 30–34 nm, 25–30 nm and 30–35 nm, respectively. The lattice parameters of CuO, MoO_3 and ZnO were calculated using Eqs. (2), (3), and (4):

$$\frac{1}{d_{hkl}^2} = (h^2 + k^2 + l^2)\frac{1}{a^2} \tag{2}$$

$$\frac{1}{d_{hkl}^2} = \frac{h^2}{a^2} + \frac{k^2}{b^2} + \frac{l^2}{c^2} \tag{3}$$

$$\frac{1}{d_{hkl}^2} = \frac{4}{3}\left[\frac{h^2 + hk + k^2}{a^2}\right] + \frac{l^2}{c^2} \tag{4}$$

where *a*, *b*, *c* are the lattice parameters, *h*, *k*, *l* are the miller indices and the d is the inter-planar spacing for the respective *h*–*k*–*l*. The inter-planar spacing is calculated using Bragg's law in $n\lambda = 2d \sin\theta$ [15].

6.2 FE-SEM analysis of CuO, MoO_3 and ZnO NCAPs

The FE-SEM images of CuO, MoO_3, and ZnO NCAPs are shown in Fig. 4a–c. The low and high magnification images of CuO-NCAP are shown in Fig. 4a. In this process, the conversion of Cu to CuO is dependent on the change in absolute temperature (1 °C/min). Moreover, the presence of oxygen plays a key role in changing the sphere-like morphological arrangement in CuO [9, 11]. The low and high magnifications of the structure of MoO_3 NCAP are shown in Fig. 4b. The combined effect of an increase in plasma power (150 W) and the substrate absolute temperature produces the plate-like morphology in MoO_3 [17]. Moreover, FE-SEM images of ZnO NCAP are shown in Fig. 4c. The effect of high substrate temperature and the oxygen ratio induces a multi-nucleation process which produces wedge-like morphology in ZnO [38].

6.3 Energy dispersive spectrum analysis

EDS and the corresponding colour mapping images are shown in Fig. 5a–f, respectively. The result is the atomic percentages of Cu (50%): O (49%) for CuO, Mo (25%): O (75%) for MoO_3 and Zn (42%): O (58%) for ZnO. It is clear that there is a homogenous distribution of Cu, Mo and Zn (red) and O (green).

6.4 UV–Vis analysis

The UV–Vis diffuse reflectance spectra of the NCAPs are shown in Fig. 6a–f. The CuO coated SS316 displays a strong reflection from 250 to 330 nm in the UV region as shown in Fig. 6a, d. Further, the band gap of CuO was estimated using a KM plot with $[F(R)hv]^{1/2}$ versus photon energy (eV) of slope to be 1.8 eV in the UV region. Similarly, Fig. 6b, e shows the UV–Vis diffuse reflectance spectra of MoO_3-NCAPs. The reflection peak and the calculated band gap energy are 430 nm and 3.2 eV. Further, Fig. 6c, f shows the ZnO-NCAPs strong reflection peak at 395 nm and band gap was 3.07 eV. The diffuse reflectance spectra for weakly absorbing samples can be expressed by the KM equation:

$$F(R) = \frac{(1-R)^2}{2R} \tag{5}$$

$$\alpha = \frac{F(R)}{t} = \frac{Absorbance}{t} \tag{6}$$

where *R* is the diffused UV reflectance, *F*(*R*) is KM function which corresponds to the absorbance, *t* is thickness and *α* is absorption coefficient. *F*(*R*) values were converted to the linear absorption coefficient. The calculated absorption coefficient of the CuO, MoO_3 and ZnO were 666.22, 552.43 and 290.79 cm^{-1}, respectively [14].

6.5 Characterization by Raman spectroscopy

The phase structure characterization of CuO, MoO_3 and ZnO-NCAPs using Raman spectra is shown in Fig. 7a–c. Raman spectra show that three Raman active phonon vibrations of the 296 cm^{-1} peak correspond to the A_g mode and the 350 and 630 cm^{-1} peaks are the B_g mode for CuO-NCAPs [26]. Also, Fig. 7a shows that the MoO_3-NCAPs have all sharp peaks that are well defined due to the highly crystalline nature of the materials. The high intense peaks identified at 822 cm^{-1} are the layered structure of symmetric and asymmetric vibrations

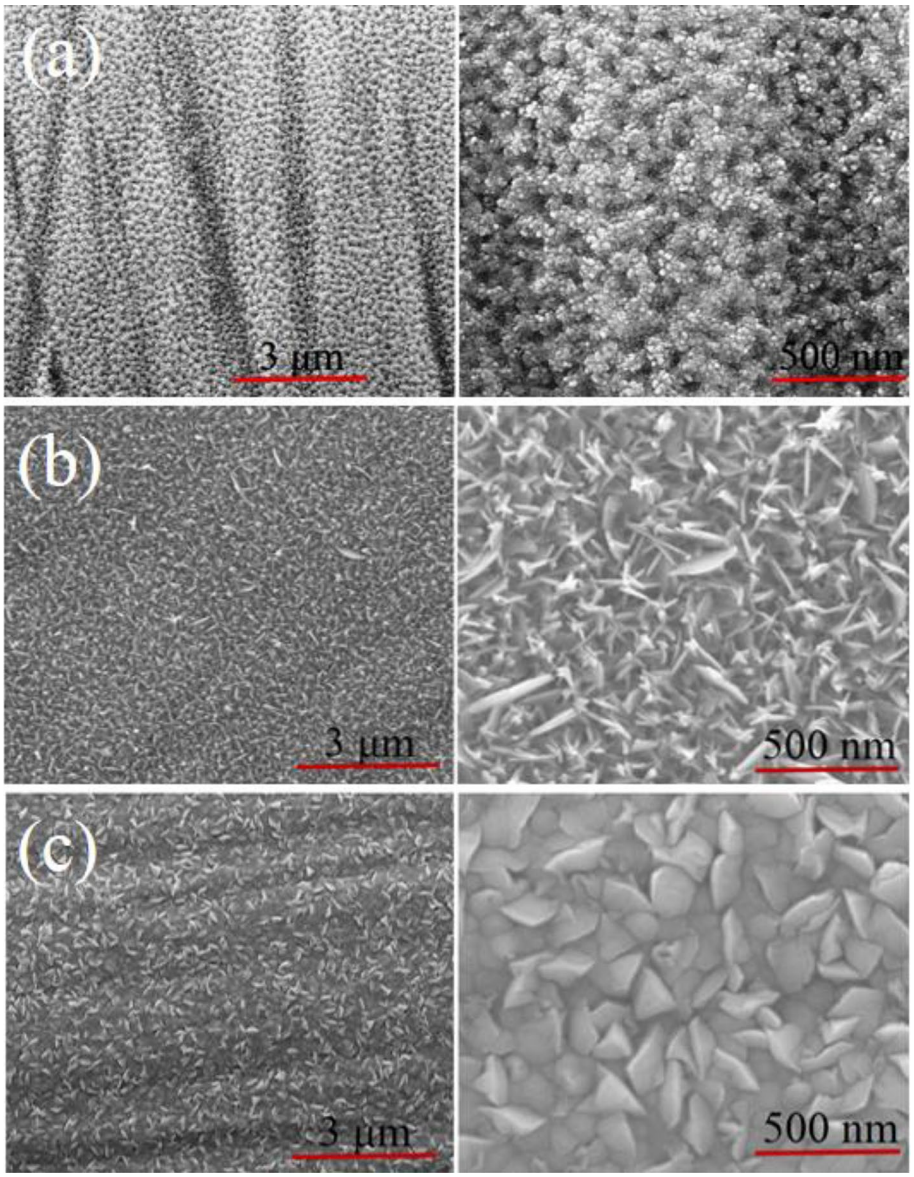

Fig. 4 FE-SEM images of **a** CuO coated NCAP, **b** MoO_3 coated NCAP, and **c** ZnO coated NCAP

of Mo–O bonds (O–Mo–O stretching modes), the band 667 and 995 cm^{-1} are due to the triply and terminal oxygen (O–Mo, Mo=O) stretching mode. The band at 130, 160, 246, 290 and 340 cm^{-1} are wagging mode of vibrations (O=Mo=O) of MoO_3 nano-sheets structure. Consequently, the peaks indicate good agreement with the orthorhombic phase of MoO_3 nanostructure sheets [43]. Furthermore, Fig. 7b reveals that the lattice and phonon vibrations due to the high crystalline E_2 (High) vibration at 437 cm^{-1} and 394 cm^{-1} belong to the A_1 (TO) mode of vibrations. The vibrations at 331 cm^{-1} peaks for $3E_{2H}$–E_{2L} correspond to multiple phonon scattering mode of ZnO coated SS316 substrate (see Fig. 7c). Finally, the substrate was thermally treated causing the peaks to be shifted slightly, and making stronger and sharper intensity in Raman spectra for XRD results [3].

6.6 Characterization of AFM

The topography was investigated using AFM and the same is shown in Fig. 8a–c. All the NCAPs were studied across 1 × 1 mm scan area. The CuO-NCAP for entire surface topography is nano-sphere like structure, with root mean square (RMS) of 120 nm height variation and average height of the nano-sphere of 1 μm (Fig. 8a). Also, the MoO_3 coated SS316 substrate had height RMS of 11 nm and average height of nano-sheet of 250 nm (Fig. 8b). Finally, ZnO-NCAP, the RMS height is 22 nm and the average height of a nano-sheet is 220 nm (Fig. 8c). The uncoated and coated NCAPs are shown in Fig. 9a–d. The properties of CuO, MoO_3 and ZnO-NCAPs are shown in Table 2.

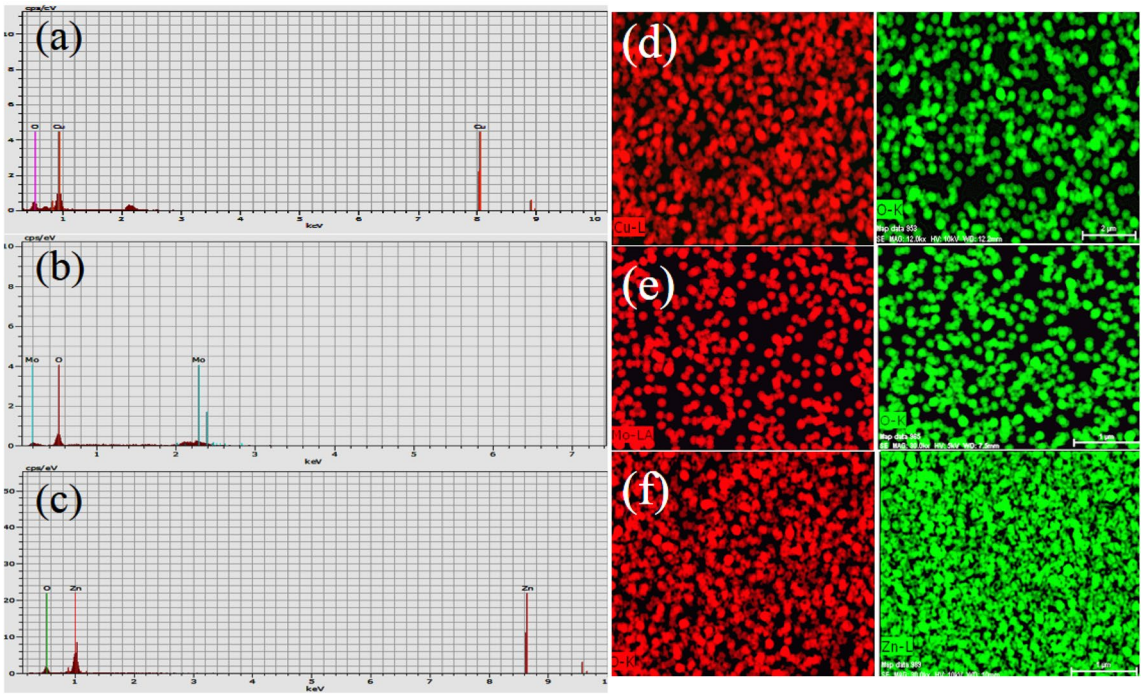

Fig. 5 EDS of CuO coated NCAP (**a**), MoO_3 coated NCAP (**b**), and ZnO coated NCAP (**c**) and colour mapping images of CuO coated NCAP (red is Cu and green is O) (**d**), MoO_3 coated NCAP (red is Mo and green is O) (**e**) and ZnO coated NCAP (red is Zn and green is O) (**f**)

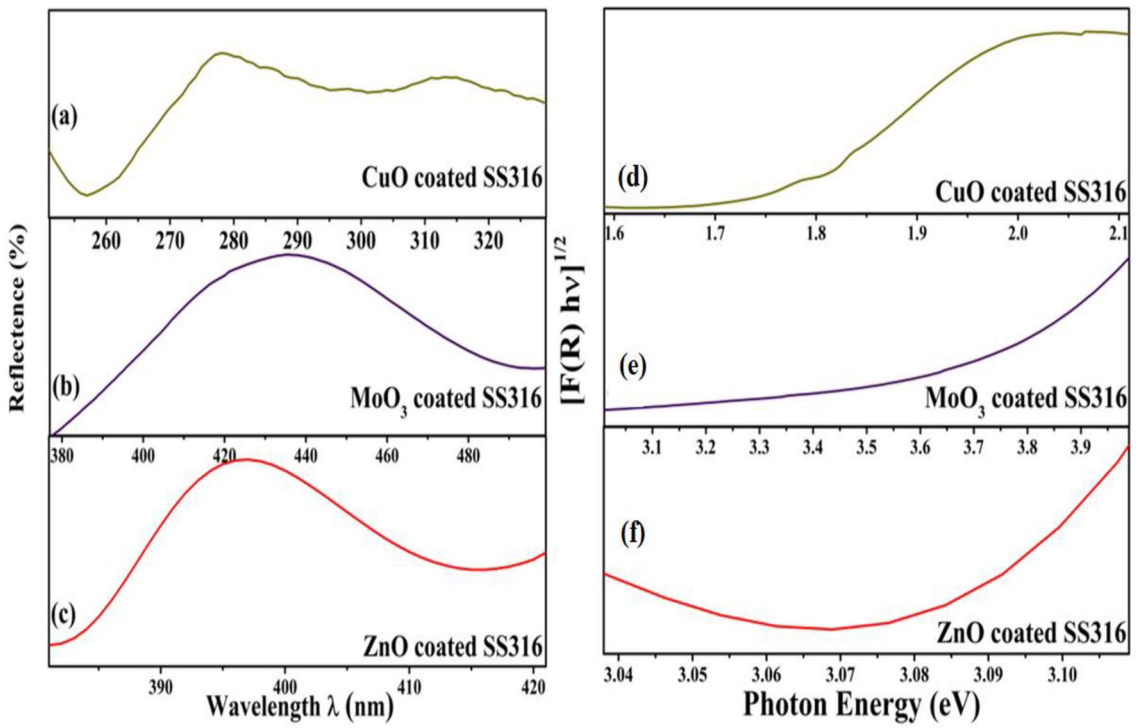

Fig. 6 Results of Diffuse UV–Vis spectra for CuO coated SS316 (**a**), MoO_3 coated SS316 (**b**), and ZnO coated SS316 (**c**) and results of KM plot vs Photon Energy of CuO coated SS316 (**d**), MoO_3 coated SS316 (**e**), and ZnO coated SS316 (**f**)

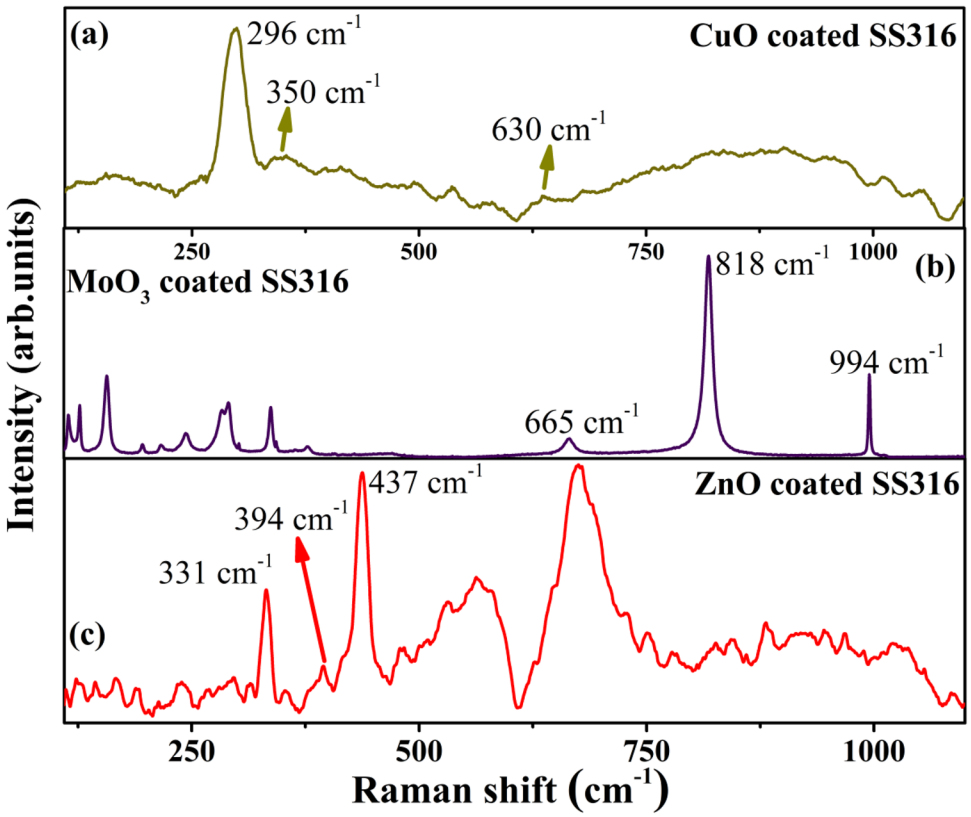

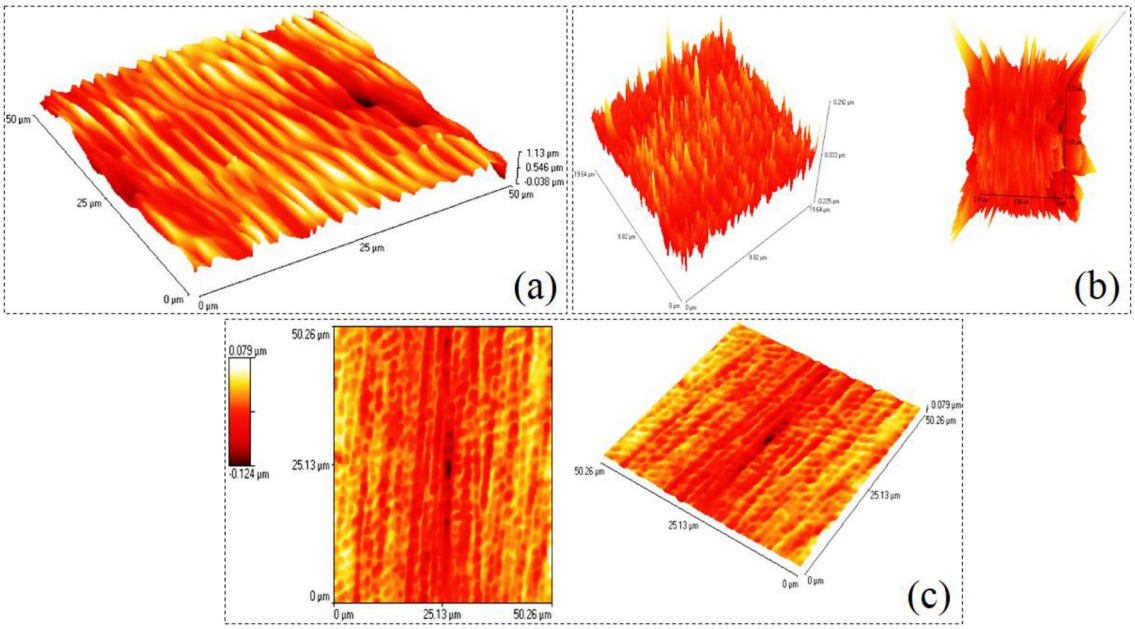

Fig. 7 Raman spectra characterization of CuO coated SS316 (**a**), MoO_3 coated SS316 (**b**) and ZnO coated SS316 (**c**)

Fig. 8 AFM characterization of CuO coated SS316 (**a**), MoO_3 coated SS316 (**b**), and ZnO coated SS316 (**c**)

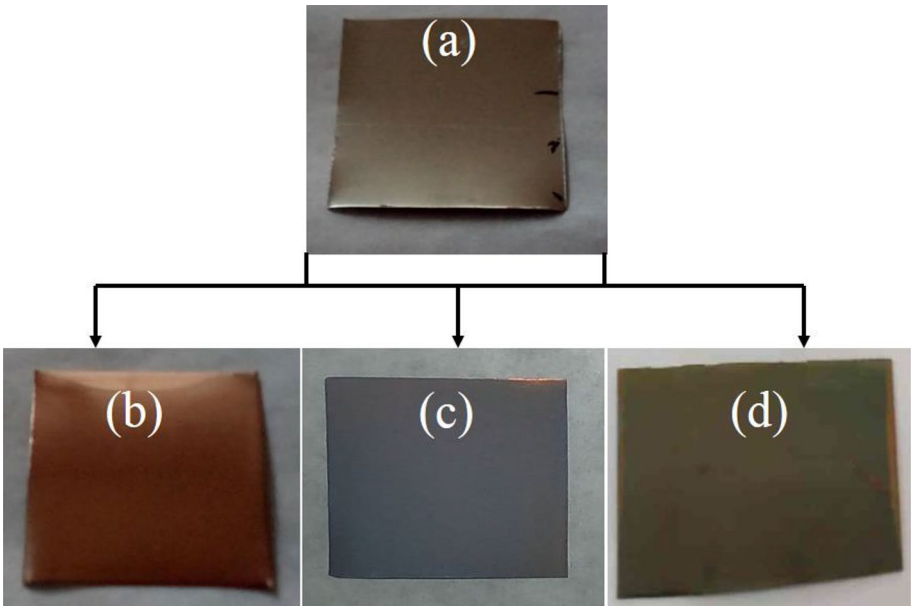

Fig. 9 Pictorial view of **a** uncoated SS316 plate, **b** CuO-NCAP, **c** MoO_3-NCAP, and **d** ZnO-NCAP

Table 2 Properties of CuO, MoO_3 and ZnO-NCAPs

S. no.	Detail of the material	CuO	MoO_3	ZnO
1.	Material	SS316	SS316	SS316
2.	Thickness of SS316 (mm)	0.1	0.1	0.1
3.	Mass of SS316 (g)	1.29	1.29	1.29
4.	Coating method	Thermal Evaporation	RF Magnetron Sputtering	RF Magnetron Sputtering
5.	Thermal conductivity (W/m. K)	76	30.7	29
6.	Density (g/cm^3)	6.4	4.6	5.6
7.	Particle size (nm)	30–34	25–30	30–35
8.	SEM morphology	Sphere	Plates	Wedges

6.7 Effect of solar radiation, ambient and wind velocity

The outdoor experiment was conducted at the rooftop of Institute for Energy studies Building, Anna University, India during the period of February 2018 to March 2018. Before the commencement of the experiment all four identical SSSSs had their inclined surface facing south to get the maximum solar influx. Figure 10 shows a photo of the experimental arrangement on the rooftop. The solar intensity, ambient temperature and wind velocity were recorded on 2018/03/22 and are shown in Fig. 11. Apart from the design aspects, the strong solar intensity, ambient conditions and appropriate wind velocity determined the productivity of the SS. The T_{amb} was measured near the SSs. The wind reduces the temperature of the top cover and enhances the condensation. The recorded solar intensity was 503.4 W/m^2 at 9:00 am and further increased to 936 W/m^2 by noon and then decreased after noon. The average solar intensity during the day was 625 W/m^2. The ambient temperature was maximum of 37 °C at noon and average ambient temperature was 34 °C. The average wind velocity was 0.63 m/s during the SS operation from 9 am to 5:30 pm. Figure 12 shows the recorded average solar radiation, T_{amb} and wind for Feb 2018 to July 2018. February to June are good for conducting solar experiments in Indian climatic conditions. The 13° South inclined SSSS directly faces the sun at solar noon on March 21. For Chennai (Latitude 13° N), at solar noon, sun will appear in the sky at a zenith angle of 10.45° North on June 21 and 36.45° south on December 21 respectively. The mean zenith solar angle lies 13° (i.e. Latitude of Chennai) towards south from the vertical.

6.8 Results of recorded temperatures in the distiller

T_w, $T_{int\text{-}air}$, T_{ic} T_{oc} of the CSSSS, SSSS-CuO, SSSS-MoO_3 and SSSS-ZnO-NCAPs are depicted in Fig. 13a–d. The

Fig. 10 Photo of experimental arrangement

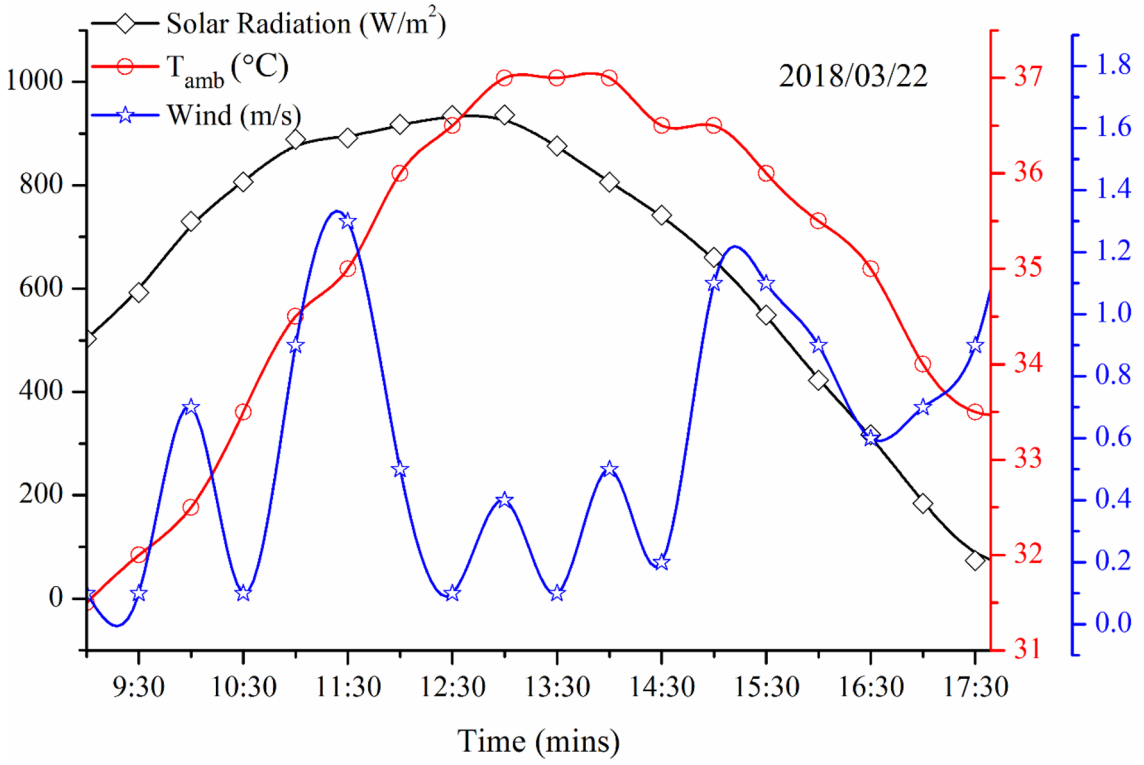

Fig. 11 Graphical view of solar radiaiton, ambient and wind

absorptivity of the basin is the prime contributor to the rise the temperature in the SSSSs [56]. Apart from that, nanomaterials in the basin influence the heat transfer in the SSSS. The materials' thermal properties and optical absorption characteristics play roles in the basin water temperature. The highest recorded T_w in the CSSSS, SSSS-CuO, SSSS-MoO_3 and SSSS-ZnO-NCAPs were 58.5 °C, 65.8 °C, 62.4 °C and 60.2 °C, respectively. The changes in the graphs are mainly due to climatic parameters like solar radiation, ambient temperature and wind.

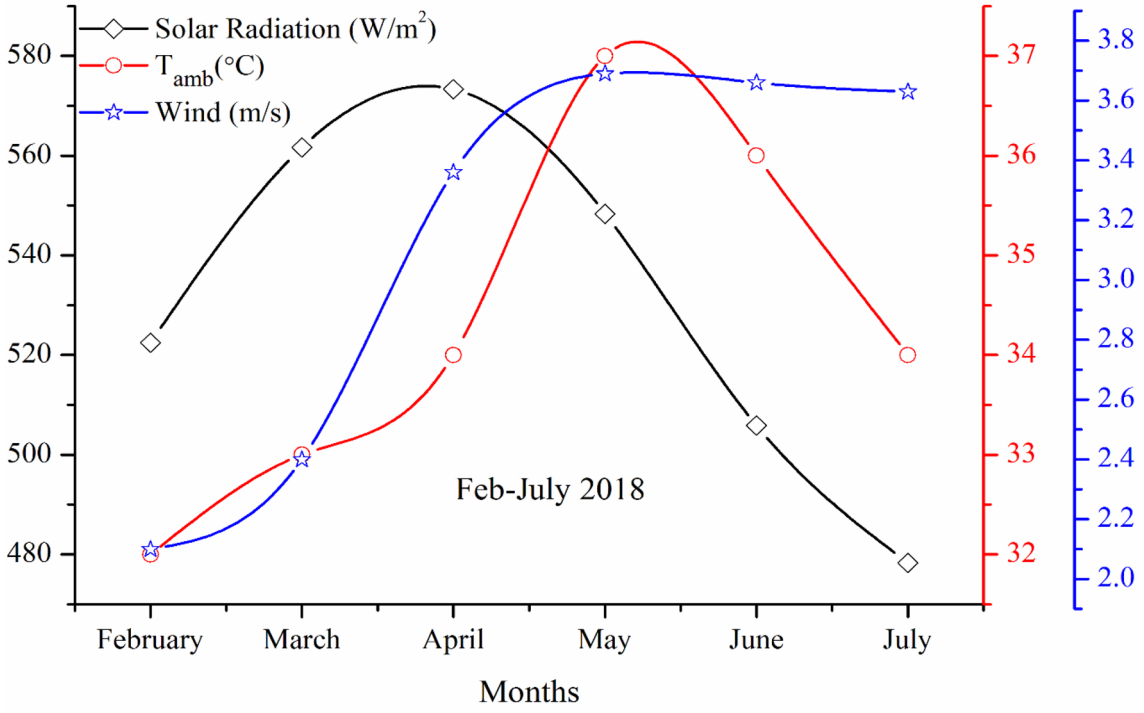

Fig. 12 The aveage solar radiation during the day on a horizontal surface, ambient and wind for the months from February to July 2018

Sometimes passing clouds causes sudden falls in the radiation and directly influence the temperature of the SS.

6.9 The CuO, MoO_3 and ZnO-NCAPs in the SSSS

The CuO, MoO_3 and ZnO-NCAP temperatures are illustrated in Fig. 14. The NCAPs were individually connected with J-type thermocouples to measure the variations in the temperature. The maximum recorded temperatures of CuO, MoO_3 and ZnO NCAPs were 64.3 °C, 61.0 °C, and 59.7 °C, respectively.

6.10 Results of evaporation rate

The evaporation rate of SSSS with NCAPs are shown in Fig. 15. A reference CSSSS also operated with the modified SSSSs to measure the enhancement level. The AFM characterization reveals that the surface roughness is higher for the CuO-NCAP than for the MoO_3 and ZnO NCAPs. The surface roughness induces multiple scattering [66] and absorption on the surface of the CuO-NCAP. At the same time, since the NCAPs are submerged, the heat energy is efficiently transferred to the bulk water in the SSSS. So adding the nanomaterial in the SSSSs efficiently enhances the basin temperature. The thermal conductivity of CuO is higher than MoO_3 and ZnO NCAPs. This may be why the CuO-NCAPs have higher productivity than the MoO_3 and ZnO-NCAPs. The productivity of the CSSSS, CuO, MoO_3 and ZnO-NCAPs were CSSSS, CuO, MoO_3 and ZnO-NCAPs were 2.1 l/m^2 day, 2.9 l/m^2 day, 2.7 l/m^2 day and 2.6 l/m^2 day, respectively. The total productivity is the sum of day and night time evaporation.

6.11 Evaporation efficiency

The evaporation efficiency of the SSSS is calculated by Arunkumar et al. [7]

$$\eta = \frac{M \times L}{I \times A \times t} \times 100 \quad (7)$$

where M is the mass of the evaporated water (kg), L is the latent heat of evaporation during the phase-change (J/kg), I is the horizontal solar influx (W/m^2), A is the horizontal area of the SSSS and t is the time (s). The calculated efficiency of the CSSSS, SSSS-CuO, SSSS-MoO_3, and SSSS-ZnO NCAPs were 23.3%, 32.1%, 30.5% and 28.9%, respectively. The CuO-NCAPs enhanced the efficiency by 38% over the CSSSS.

6.12 Heat transfer coefficients

The heat transfer coefficients are calculated as follows:

The convective heat transfer coefficient between water and glass is estimated as [36],

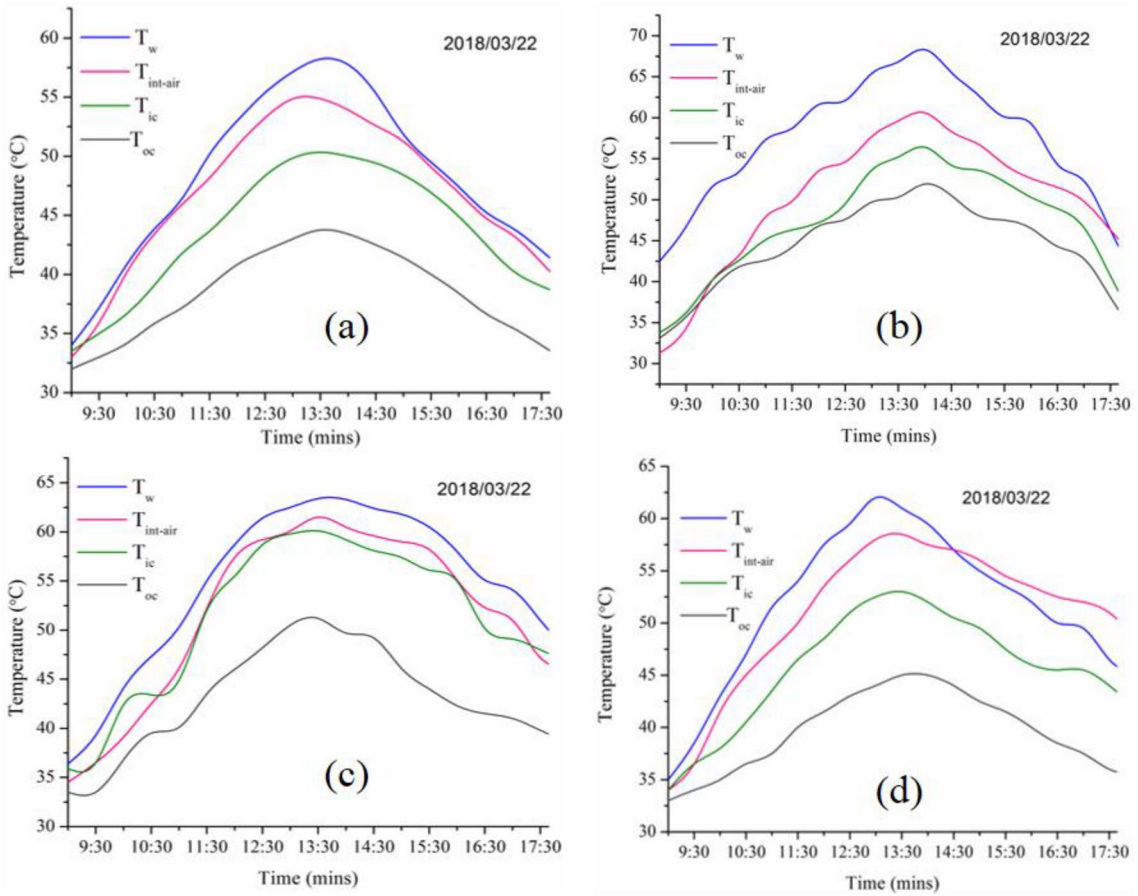

Fig. 13 Recorded temperature profile of CSSSS (**a**), SSSS-CuO (**b**), SSSS-MoO_3 (**c**) and SSSS-ZnO NCAPs (**d**)

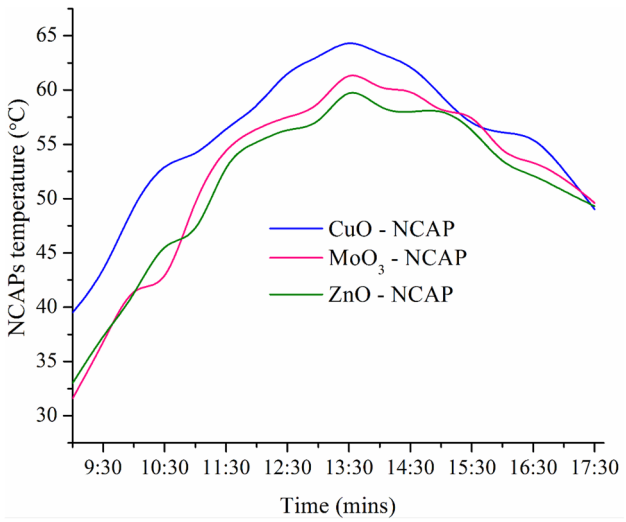

Fig. 14 Recorded temperatures of CuO, MoO_3 and ZnO-NCAPs

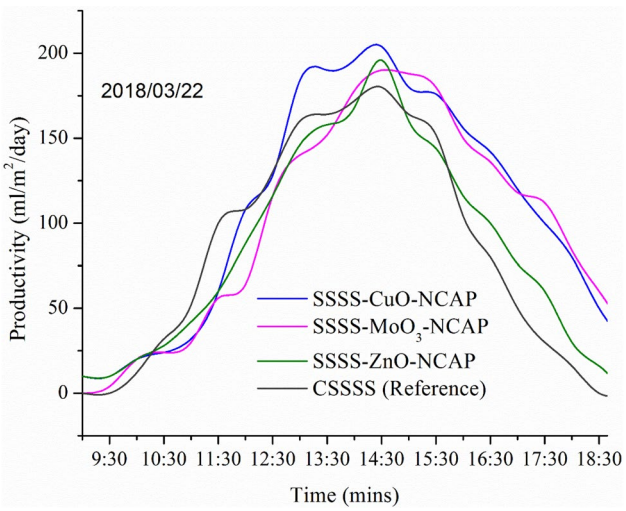

Fig. 15 Fresh water productivity of CuO, MoO_3, ZnO-NCAPs and CSSSS

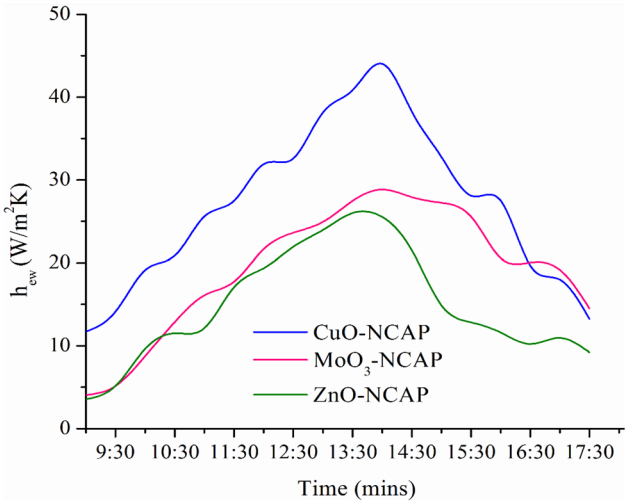

Fig. 16 Evaporation heat transfer coefficient of CuO, MoO_3 and ZnO-NCAPs

$$h_{c,w-ic} = 0.884\left[\left(T_w - T_{ic}\right) + \frac{\left(T_w + 273.15\right)\left(p_w - p_{ic}\right)}{\left(268900 - p_w\right)}\right]^{1/3} \tag{8}$$

The evaporative heat transfer coefficient between water and glass is given as [59],

$$h_{e,w-ic} = 16.27 \times 10^{-3} \times h_{c,w-ic}\left[\frac{\left(P_w - P_{ic}\right)}{\left(T_w - T_{ic}\right)}\right] \tag{9}$$

The radiative heat transfer coefficient between water and glass is given as [36],

$$h_{r,w-ic} = \varepsilon_{effective}\sigma\left[\left(T_w + 273.15\right)^2 + \left(T_{ic} + 273.15\right)^2\right]\left[T_w + T_{ic} + 546\right] \tag{10}$$

where,

$$\varepsilon_{effective} = \left(\frac{1}{\frac{1}{\varepsilon_{ic}} + \frac{1}{\varepsilon_w} - 1}\right) \tag{11}$$

The convective heat transfer coefficient from the SSSS cover to ambient is calculated as [59],

$$h_{c,oc-amb} = 5.7 + 3.8u \tag{12}$$

The radiative heat transfer coefficient to ambient is estimated as [59],

$$h_{r,oc-amb} = \varepsilon_{effective}\sigma\left[\left(T_{oc} + 273.15\right)^2 + \left(T_{amb} + 273.15\right)^2\right]\left[T_{oc} + T_{amb} + 546\right] \tag{13}$$

where

Table 3 The physical and chemical water quality analysis

S. no.	Test parameters	Unit	SWW (BT)	SWW (AT)	HWW (BT)	HWW (AT)	HPW (BT)	HPW (AT)	IS 10500-2012 Drinking water	
									Acceptable limit	Permissible limit
1	pH	–	7.1	6.5	6.9	6.38	7	6.85	6.5–8.5	NR
2	Electrical conductivity	µS/cm	1099	33	230	15	450	8	–	–
3	Turbidity	NTU	2	0.2	5	1	8	0.8	1	5
4	Total dissolved solids	mg/l	846	25	500	25	299	21	500	2000
5	Total alkalinity	mg/l	380	14	200	16	140	16	200	600
6	Total hardness	mg/l	520	12	200	21	150	12	200	600
7	Calcium as Ca	mg/l	280	3.21	75	6	30	2	75	200
8	Magnesium as Mg	mg/l	58	0.97	30	1	18	1	30	100
9	Chloride Cl	mg/l	130	6	22	3	30	2	250	1000
10	Sulphate as SO_4	mg/l	163	6	12	0.2	1.4	0.3	200	400
11	Iron as Fe	mg/l	0.64	0.58	0.16	0.1	BDL	0	0.3	NR
12	$CaCO_3$	mg/l	40	2	10	0.3	10	0.1	–	–
13	Fluoride as F	mg/l	0.76	0.01	0.35	0	0.44	0	1	1.5
14	Nitrate as NO_3	mg/l	0.93	0.58	6.4	2	BDL	0	45	NR

$$p_w = e^{\left(25.314-\frac{5144}{T_w+273.15}\right)}$$

$$p_c = e^{\left(25.314-\frac{5144}{T_{ic}+273.15}\right)}$$

Figure 16 shows the evaporation heat transfer coefficient (h_{ew}) of SSSS-NCAPs. The calculated evaporation heat transfer for SSSS-CuO, SSSS-MoO_3, and SSSS-ZnO-NCAPs were 43.1 W/m^{2}K, 28.84 W/m^{2}K, and 25.53 W/m^{2}K, respectively.

6.13 Physical and chemical water quality analysis

The physical and chemical water quality results are illustrated in Table 3. Three different water samples were evaporated by the CuO-NCAPs. Among the three samples, one of them was fetched from the surface well water (SWW) which was situated near the industrial area of Kanjikode, Kerala state of India and other two samples were fetched from 4920 m high Palamalai mountains (11.00° N and 77.97° E) open pond water (HPW) and well water (HWW). The water quality test (Ref. No. 31-4098/2018-19) was carried-out at the Kerala Water Authority, Quality Control District Laboratory, Palakkad, India. The result concluded that the water quality was improved after evaporation and found acceptable according to the range prescribed by the Indian standard (IS 10500-2012).

Table 4 Cost analysis of solar still with absorbing materials (*NA* not applicable)

US$	CSSSS	SSSS with CuO-NCAP	SSSS with MoO_3-NCAP	SSSS with ZnO-NCAP
Galvanized iron	30	30	30	30
Top cover	6	6	6	6
Black paint	3	3	3	3
Fresh water port	2	2	2	2
Bubble wrap	1.55	1.55	1.55	1.55
CuO-NCAP	NA	8	NA	NA
MoO_3-NCAP	NA	NA	9	NA
ZnO-NCAP	NA	NA	NA	5
Pipes	2	2	2	2
Labour charge	15	15	15	15
Totals (USD)	59.55	67.55	68.55	64.55
L/m^2/day (USD)	2.1	2.9	2.75	2.6
$/L water (USD)	0.0097	0.0080	0.0085	0.0085

6.14 Comparison of results with recent in nano-enabled SSs

Many researchers have used NPs in different ways in SSs to enhance the freshwater productivity (see Fig. 17). NPs have been doped into black paint [33], mixed with bulk water as a NF [19, 29, 30, 45]; Sahota and Tiwari [49, 50], integrated with phase change materials (PCM) [27, 28, 54] and coated on the substrate [9, 11]. Apart from that, various NPs have been used as a NF to improve the

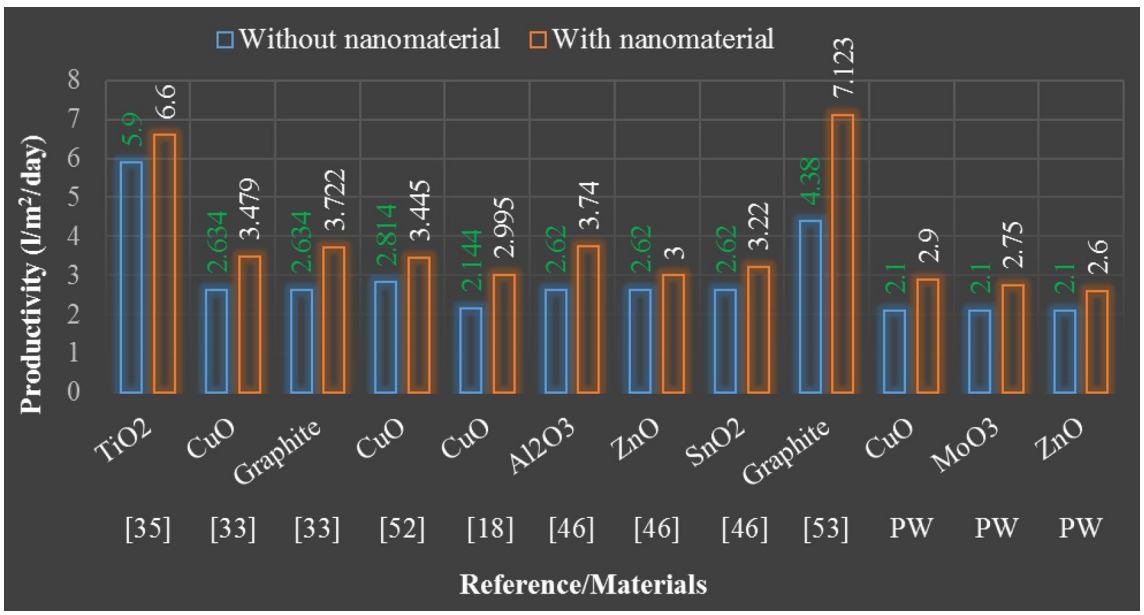

Fig. 17 Comparison of various nanomaterials in the SS with present work (PW)

efficiency of the SS. Researchers experimented with the following NFs: CuO [21], Al_2O_3 [19], SnO_2 [19], ZnO [19] and graphite [31] and they found that the NF improved the performance of the SS. The NPs in the SSs increased the basin absorptance and transferred the heat to the bulk water.

6.15 Economic analysis

The cost of various components of the SSSSs are shown in Table 4. The cost of the CSSSS and SSSS with CuO, MoO_3 and ZnO NCAPs were $59.55, $67.55, $68.04 and $64.55, respectively. The SSSS-CuO NCAP with an output of 2.9 l/m^2/day, a life of 15 years, an equivalent of 80% sunny days and interest of 6% yields approximately $0.0080/L. Similarly, it is $0.0097/L for CSSSS, $0.0085/L for SSSS-$MoO_3$ NCAP and $0.0085/L for SSSS-ZnO NCAP. Thus, the SSSS-CuO NCAP has the lowest cost of water.

7 Concluding remarks

In summary, three nano-enabled absorbers CuO, MoO_3 and ZnO were examined in SSSSs under natural solar influx. The NCAPs were allowed to contact directly with the water to transfer heat. The prepared NCAPs were characterized by the XRD, FE-SEM, EDS-colour mapping, UV–Vis, Raman spectroscopy, and AFM analyses. Three different water samples were examined in the SSSSs. The distilled output of the CSSSS, CuO, MoO_3 and ZnO NCAPs were CSSSS, CuO, MoO_3 and ZnO NCAPs were 2.1 l/m^2 day, 2.9 l/m^2 day, 2.7 l/m^2 day and 2.6 l/m^2 day, respectively. Similarly, the calculated evaporation efficiencies of the CSSSS, CuO, MoO_3 and ZnO NCAPs were 23.3%, 32.1%, 30.5% and 28.9%, respectively. The evaporation heat transfer coefficient of the CuO-NCAPs was higher (43.1 W/m^2 K) than the MoO_3 and ZnO NCAPs. Therefore, the CuO-NCAPs has the highest productivity and efficiency. The CuO-NCAPs enhanced the thermal conductivity and heat transfer of the basin due to their rough surface. The coated NPs on the substrate absorbed the incoming solar radiation due to multiple scattering. There was more reflection due to the smooth surface of the MoO_3 and ZnO NCAPs. Finally, the physical and chemical tests reveal that the water quality was improved after evaporation and found within the limit of IS 10500-2012 drinking water quality standards.

8 Future work

To increase the evaporation rate of wastewater in the SSSS, natural hydrophilic porous materials such as wood and leaves could be carbonized. The carbonized wood and leaves would be capable of absorbing the incoming solar radiation (broadband absorption) perhaps better than conventional absorbers. These materials could also act as sensible heat storage.

Acknowledgements This study received grant from University Grant Commission (UGC), Government of India. Ref. No. F.4-2/2016 (BSR)/PH/14-15/0124 dated on 01 July 2016.

Compliance with ethical standards

Conflict of interest There are no conflicts of interest to declare.

References

1. Agrawal A, Rana RS, Srivastava PK (2018) Application of jute cloth (natural fibre) to enhance the distillate output in solar distillation system. Mater Today Proc 5:4893–4902. https://doi.org/10.1016/j.matpr.2017.12.066
2. Ali N, Kamal T, Ul-Islam M, Khan A, Shah SJ, Zada A (2018) Chitosan-coated cotton cloth supported copper nanoparticles for toxic dye reduction. Int J Biol Macromol 111:832–838. https://doi.org/10.1016/j.ijbiomac.2018.01.092
3. Allen JA, Murugesan D, Viswanathan C (2019) Circumferential growth of zinc oxide nanostructure anchored over carbon fabric and its photocatalytic performance towards p-nitrophenol. Superlattices Microstruct 125:159–167. https://doi.org/10.1016/j.spmi.2018.11.007
4. Arjunan TGSTV (2018) Thermodynamic performance comparison of single slope solar stills with and without cotton cloth energy storage medium. J Therm Anal Calorim. https://doi.org/10.1007/s10973-018-7909-0
5. Arunkumar T, Denkenberger D, Velraj R, Sathyamurthy R, Tanaka H, Vinothkumar K (2015) Experimental study on a parabolic concentrator assisted solar desalting system. Energy Convers Manag. https://doi.org/10.1016/j.enconman.2015.08.021
6. Arunkumar T, Jayaprakash R, Ahsan A, Denkenberger D, Okundamiya MS (2013) Effect of water and air flow on concentric tubular solar water desalting system. Appl Energy 103:109–115. https://doi.org/10.1016/j.apenergy.2012.09.014
7. Arunkumar T, Jayaprakash R, Denkenberger D, Ahsan A, Okundamiya MS, Kumar S, Tanaka H, Aybar HŞ (2012) An experimental study on a hemispherical solar still. Desalination 286:1–2. https://doi.org/10.1016/j.desal.2011.11.047
8. Arunkumar T, Kabeel AE, Raj K, Denkenberger D, Sathyamurthy R, Ragupathy P, Velraj R (2018) Productivity enhancement of solar still by using porous absorber with bubble-wrap insulation. J Clean Prod. https://doi.org/10.1016/j.jclepro.2018.05.199

9. Arunkumar T, Murugesan D, Raj K, Denkenberger D, Viswanathan C, Rufuss DDW, Velraj R (2019) Effect of nano-coated CuO absorbers with PVA sponges in solar water desalting system. Appl Therm Eng. https://doi.org/10.1016/j.applthermaleng.2018.10.129
10. Arunkumar T, Raj K, Denkenberger D, Velraj R (2018) Heat carrier nanofluids in solar still: a review. Desalin Water Treat 22:1–16. https://doi.org/10.5004/dwt.2018.22972
11. Arunkumar T, Raj K, Dsilva Winfred Rufuss D, Denkenberger D, Tingting G, Xuan L, Velraj R (2019) A review of efficient high productivity solar stills. Renew Sustain Energy Rev 101:197–220. https://doi.org/10.1016/j.rser.2018.11.013
12. Arunkumar T, Velraj R, Denkenberger D, Sathyamurthy R, Vinothkumar K, Porkumaran K, Ahsan A (2016) Effect of heat removal on tubular solar desalting system. Desalination 379:24–33. https://doi.org/10.1016/j.desal.2015.10.007
13. Arunkumar T, Velraj R, Denkenberger DC, Sathyamurthy R (2016) Influence of crescent shaped absorber in water desalting system. Desalination 398:208–213. https://doi.org/10.1016/j.desal.2016.07.039
14. Aydın C, Al-Hartomy OA, Al-Ghamdi AA, Al-Hazmi F, Yahia IS, El-Tantawy F, Yakuphanoglu F (2012) Controlling of crystal size and optical band gap of CdO nanopowder semiconductors by low and high Fe contents. J Electroceram 29:155–162. https://doi.org/10.1007/s10832-012-9748-x
15. Cullity BD (1978) Elements of X-ray diffraction, 2nd edn. Addison-Wesley Publishing Company Inc., Phillippines
16. Cheng W, Huo Y, Nian Y (2019) Performance of solar still using shape-stabilized PCM: experimental and theoretical investigation. Desalination 455:89–99. https://doi.org/10.1016/j.desal.2019.01.007
17. Chithambararaj A, Rajeswari Yogamalar N, Bose AC (2016) Hydrothermally synthesized h-MoO_3 and α-MoO_3 nanocrystals: new findings on crystal-structure-dependent charge transport. Cryst Growth Des 16:1984–1995. https://doi.org/10.1021/acs.cgd.5b01571
18. Du Y, Wu Q, Lv X, Wang Q, Lu Y, Hu H (2018) Exposure to solar light reduces cytotoxicity of sewage effluents to mammalian cells: roles of reactive oxygen and nitrogen species. Water Res 143:570–578. https://doi.org/10.1016/j.watres.2018.07.014
19. Elango T, Kannan A, Kalidasa Murugavel K (2015) Performance study on single basin single slope solar still with different water nanofluids. Desalination 360:45–51. https://doi.org/10.1016/j.desal.2015.01.004
20. Gong F, Li H, Wang W, Huang J, Xia D, Liao J, Wu M, Papavassiliou DV (2019) Scalable, eco-friendly and ultrafast solar steam generators based on one-step melamine-derived carbon sponges toward water purification. Nano Energy 58:322–330. https://doi.org/10.1016/j.nanoen.2019.01.044
21. Gupta B, Shankar P, Sharma R, Baredar P (2016) Performance enhancement using nano particles in modified passive solar still. Procedia Technol 25:1209–1216. https://doi.org/10.1016/j.protcy.2016.08.208
22. Hansen RS, Narayanan CS, Murugavel KK (2015) Performance analysis on inclined solar still with different new wick materials and wire mesh. Desalination 358:1–8. https://doi.org/10.1016/j.desal.2014.12.006
23. Hong X, Li S, Wang R, Fu J (2019) Hierarchical SnO2 nanoclusters wrapped functionalized carbonized cotton cloth for symmetrical supercapacitor. J Alloys Compd 775:15–21. https://doi.org/10.1016/j.jallcom.2018.10.099
24. Ibarra-taquez HN, Gilpavas E, Blatchley ER, Angel M (2017) Integrated electrocoagulation-electrooxidation process for the treatment of soluble coffee of fluent: optimization of COD degradation and operation time analysis. J Environ Manag 200:530–538. https://doi.org/10.1016/j.jenvman.2017.05.095
25. Janhom S (2019) Effect of consecutive $SiCl_4$ and hydrophobic molecule modification of cotton cloth for fresh oils and used oils removal. J Environ Chem Eng 7:103120. https://doi.org/10.1016/j.jece.2019.103120
26. Jayram ND, Aishwarya D, Sonia S, Mangalaraj D, Kumar PS, Rao GM (2016) Analysis on superhydrophobic silver decorated copper Oxide nanostructured thin films for SERS studies. J Colloid Interface Sci 477:209–219. https://doi.org/10.1016/j.jcis.2016.05.051
27. Kabeel AE, Abdelgaied M, Eisa A (2018) Effect of graphite mass concentrations in a mixture of graphite nanoparticles and paraffin wax as hybrid storage materials on performances of solar still. Renew Energy. https://doi.org/10.1016/j.renene.2018.07.147
28. Kabeel AE, El-Agouz SA, Sathyamurthy R, Arunkumar T (2018) Augmenting the productivity of solar still using jute cloth knitted with sand heat energy storage. Desalination 443:122–129. https://doi.org/10.1016/j.desal.2018.05.026
29. Kabeel AE, Omara ZM, Essa FA (2017) Numerical investigation of modified solar still using nanofluids and external condenser. J Taiwan Inst Chem Eng 75:77–86. https://doi.org/10.1016/j.jtice.2017.01.017
30. Kabeel AE, Omara ZM, Essa FA (2014) Enhancement of modified solar still integrated with external condenser using nanofluids: an experimental approach. Energy Convers Manag 78:493–498. https://doi.org/10.1016/j.enconman.2013.11.013
31. Kabeel AE, Omara ZM, Essa FA (2014) Improving the performance of solar still by using nanofluids and providing vacuum. Energy Convers Manag 86:268–274. https://doi.org/10.1016/j.enconman.2014.05.050
32. Kabeel AE, Sathyamurthy R, Manokar AM, Sharshir SW, Essa FA, Elshiekh AH (2020) Experimental study on tubular solar still using Graphene Oxide Nano particles in Phase Change Material (NPCM's) for fresh water production. J Energy Storage 28:101204. https://doi.org/10.1016/j.est.2020.101204
33. Kabeel AE, Sathyamurthy R, Sharshir SW, Muthumanokar A, Panchal H, Prakash N, Prasad C, Nandakumar S, El Kady MS (2019) Effect of water depth on a novel absorber plate of pyramid solar still coated with TiO_2 nano black paint. J Clean Prod 213:185–191. https://doi.org/10.1016/j.jclepro.2018.12.185
34. Karimi Estahbanati MR, Ahsan A, Feilizadeh Mehrzad, Jafarpur K, Ashrafmansouri SS, Feilizadeh Mansoor (2016) Theoretical and experimental investigation on internal reflectors in a single-slope solar still. Appl Energy 165:537–547. https://doi.org/10.1016/j.apenergy.2015.12.047
35. Kou H, Liu Z, Zhu B, Macharia DK, Ahmed S, Wu B, Zhu M, Liu X, Chen Z (2019) Recyclable CNT-coupled cotton fabrics for low-cost and efficient desalination of seawater under sunlight. Desalination 462:29–38. https://doi.org/10.1016/j.desal.2019.04.005
36. Kumar S, Tiwari GN (2009) Estimation of internal heat transfer coefficients of a hybrid (PV/T) active solar still. Sol Energy 83:1656–1667. https://doi.org/10.1016/j.solener.2009.06.002
37. Lai CC, Chang CJ, Huang YS, Chang WC, Tseng FG, Chueh YL (2015) Desalination of saline water by nanochannel arrays through manipulation of electrical double layer. Nano Energy 12:394–400. https://doi.org/10.1016/j.nanoen.2014.10.039
38. Li Haili, Jiao S, Gao S, Li Hongtao, Li L (2014) Dynamically controlled synthesis of different ZnO nanostructures by a surfactant-free hydrothermal method. CrystEngComm 16:9069–9074. https://doi.org/10.1039/c4ce01282h
39. Li Y, Gao T, Yang Z, Chen C, Kuang Y, Song J, Jia C, Hitz EM, Yang B, Hu L (2017) Graphene oxide-based evaporator with one-dimensional water transport enabling high-efficiency solar desalination. Nano Energy 41:201–209. https://doi.org/10.1016/j.nanoen.2017.09.034

40. Mahian O, Kianifar A, Heris SZ, Wen D, Sahin AZ, Wongwises S (2017) Nanofluids effects on the evaporation rate in a solar still equipped with a heat exchanger. Nano Energy 36:134–155. https://doi.org/10.1016/j.nanoen.2017.04.025
41. Modi KV, Modi JG (2019) Performance of single-slope double-basin solar stills with small pile of wick materials. Appl Therm Eng 149:723–730. https://doi.org/10.1016/j.applthermaleng.2018.12.071
42. Mohamed AF, Hegazi AA, Sultan GI, El-Said EMS (2019) Augmented heat and mass transfer effect on performance of a solar still using porous absorber: experimental investigation and exergetic analysis. Appl Therm Eng 150:1206–1215. https://doi.org/10.1016/j.applthermaleng.2019.01.070
43. Murugesan D, Prakash S, Ponpandian N, Manisankar P, Viswanathan C (2019) Two dimensional α-MoO 3 nanosheets decorated carbon cloth electrodes for high-performance supercapacitors. Colloids Surf A Physicochem Eng Asp 569:137–144. https://doi.org/10.1016/j.colsurfa.2019.02.062
44. Nazari S, Safarzadeh H, Bahiraei M (2018) Performance improvement of a single slope solar still by employing thermoelectric cooling channel and copper oxide nanofluid: an experimental study. J Clean Prod. https://doi.org/10.1016/j.jclepro.2018.10.194
45. Omara ZM, Kabeel AE, Essa FA (2015) Effect of using nanofluids and providing vacuum on the yield of corrugated wick solar still. Energy Convers Manag 103:965–972. https://doi.org/10.1016/j.enconman.2015.07.035
46. Panchal H, Mohan I (2017) Various methods applied to solar still for enhancement of distillate output. Desalination 415:76–89. https://doi.org/10.1016/j.desal.2017.04.015
47. Rajaseenivasan T, Prakash R, Vijayakumar K, Srithar K (2017) Mathematical and experimental investigation on the influence of basin height variation and stirring of water by solar PV panels in solar still. Desalination 415:67–75. https://doi.org/10.1016/j.desal.2017.04.010
48. Rufuss DDW, Suganthi L, Iniyan S, Davies PA (2018) Effects of nanoparticle-enhanced phase change material (NPCM) on solar still productivity. J Clean Prod. https://doi.org/10.1016/j.jclepro.2018.04.201
49. Sahota Lovedeep, Tiwari GN (2016) Effect of Al2O3 nanoparticles on the performance of passive double slope solar still. Sol Energy 130:260–272. https://doi.org/10.1016/j.solener.2016.02.018
50. Sahota L, Tiwari GN (2016) Effect of nanofluids on the performance of passive double slope solar still: a comparative study using characteristic curve. Desalination 388:9–21. https://doi.org/10.1016/j.desal.2016.02.039
51. Samuel Hansen R, Kalidasa Murugavel K (2017) Enhancement of integrated solar still using different new absorber configurations: an experimental approach. Desalination 422:59–67. https://doi.org/10.1016/j.desal.2017.08.015
52. Satori H, Kawase Y (2014) Decolorization of dark brown colored coffee ef fl uent using zinc oxide particles: the role of dissolved oxygen in degradation of colored compounds. J Environ Manag 139:172–179. https://doi.org/10.1016/j.jenvman.2014.02.032
53. Selvaraj K, Natarajan A (2018) Factors influencing the performance and productivity of solar stills—a review. Desalination 435:181–187. https://doi.org/10.1016/j.desal.2017.09.031
54. Sharshir SW, Peng G, Elsheikh AH, Edreis EMA (2018) Energy and exergy analysis of solar stills with micro/nano particles: a comparative study. Energy Convers Manag 177:363–375. https://doi.org/10.1016/j.enconman.2018.09.074
55. Shukla DL, Modi KV (2019) Hybrid solar still—liquid desiccant regenerator and water distillation system. Sol Energy 182:117–133. https://doi.org/10.1016/j.solener.2019.02.043
56. Siregar MA, Damanik WS (2020) Energy analysis desalination of single slope solar still. IOP Conf Ser Mater Sci Eng. https://doi.org/10.1088/1757-899X/821/1/012046
57. Suganya S, Kumar PS (2018) Journal of Industrial and Engineering Chemistry In fl uence of ultrasonic waves on preparation of active carbon from coffee waste for the reclamation of effluents containing Cr(VI) ions. J Ind Eng Chem 60:418–430. https://doi.org/10.1016/j.jiec.2017.11.029
58. Suneesh PU, Jayaprakash R, Arunkumar T, Denkenberger D (2014) Effect of air flow on "V" type solar still with cotton gauze cooling. Desalination 337:1–5. https://doi.org/10.1016/j.desal.2013.12.035
59. Tiwari GN, Kumar S, Sharma PB, Emran Khan M (1996) Instantaneous thermal efficiency of an active solar still. Appl Therm Eng 16:189–192. https://doi.org/10.1016/1359-4311(95)00053-G
60. Tokumura M, Ohta A, Znad HT, Kawase Y (2006) UV light assisted decolorization of dark brown colored coffee effluent by photo-Fenton reaction. Water Res 40:3775–3784. https://doi.org/10.1016/j.watres.2006.08.012
61. Tokumura M, Znad HT, Kawase Y (2008) Decolorization of dark brown colored coffee effluent by solar photo-Fenton reaction: effect of solar light dose on decolorization kinetics. Water Res 42:4665–4673. https://doi.org/10.1016/j.watres.2008.08.007
62. Tomizawa M, Kurosu S, Kobayashi M, Kawase Y (2016) Zero-valent iron treatment of dark brown colored coffee ef fl uent: contributions of a core-shell structure to pollutant removals. J Environ Manag 183:478–487. https://doi.org/10.1016/j.jenvman.2016.08.081
63. Torkian L, Azimirad R, Safa S (2018) Investigating the effects of fe dopant on structural, optical, and photocatalytic properties of zno nanoflowers. Desalin Water Treat 123:196–202. https://doi.org/10.5004/dwt.2018.22682
64. Wan C, Jiao Y, Liang D, Wu Y, Li J (2018) A high-performance, all-textile and spirally wound asymmetric supercapacitors based on core e sheath structured MnO_2 nanoribbons and cotton-derived carbon cloth. Electrochim Acta 285:262–271. https://doi.org/10.1016/j.electacta.2018.07.036
65. Wang H, Zhu Q, Ding Z, Li Z, Zheng H, Fu J, Diao C, Zhang X, Tian J, Zi Y (2019) A fully-packaged ship-shaped hybrid nanogenerator for blue energy harvesting toward seawater self-desalination and self-powered positioning. Nano Energy 57:616–624. https://doi.org/10.1016/j.nanoen.2018.12.078
66. Wang X, He Y, Liu X, Cheng G, Zhu J (2017) Solar steam generation through bio-inspired interface heating of broadband-absorbing plasmonic membranes. Appl Energy 195:414–425. https://doi.org/10.1016/j.apenergy.2017.03.080
67. Wilson HM, Rahman ARS, Parab AE, Jha N (2019) Ultra-low cost cotton based solar evaporation device for seawater desalination and waste water purification to produce drinkable water. Desalination 456:85–96. https://doi.org/10.1016/j.desal.2019.01.017
68. Xu J, Xu F, Qian M, Li Z, Sun P, Hong Z, Huang F (2018) Copper nanodot-embedded graphene urchins of nearly full-spectrum solar absorption and extraordinary solar desalination. Nano Energy 53:425–431. https://doi.org/10.1016/j.nanoen.2018.08.067
69. Yi L, Ci S, Luo S, Shao P, Hou Y, Wen Z (2017) Scalable and low-cost synthesis of black amorphous Al-Ti-O nanostructure for high-efficient photothermal desalination. Nano Energy 41:600–608. https://doi.org/10.1016/j.nanoen.2017.09.042
70. Yin Z, Wang H, Jian M, Li Y, Xia K, Zhang M, Wang C, Wang Q, Ma M, Zheng Q, Zhang Y (2017) Extremely black vertically aligned carbon nanotube arrays for solar steam generation. ACS Appl Mater Interfaces. https://doi.org/10.1021/acsami.7b08619
71. Zanganeh P, Goharrizi AS, Ayatollahi S, Feilizadeh M (2020) Nano-coated condensation surfaces enhanced the productivity of the single-slope solar still by changing the condensation

mechanism. J Clean Prod 265:121758. https://doi.org/10.1016/j.jclepro.2020.121758
72. Zhang C, Bhoyate S, Hyatt M, Neria BL, Siam K, Kahol PK, Ghimire M, Mishra SR, Perez F, Gupta RK (2018) Nitrogen-doped flexible carbon cloth for durable metal free electrocatalyst for overall water splitting. Surf Coat Technol 347:407–413. https://doi.org/10.1016/j.surfcoat.2018.05.021
73. Zong L, Li M, Li C (2018) Intensifying solar-thermal harvest of low-dimension biologic nanostructures for electric power and solar desalination. Nano Energy 50:308–315. https://doi.org/10.1016/j.nanoen.2018.05.042